




Loss of Tmem106b exacerbates FTLD pathologies and causes motor deficits in progranulin-deficient mice

Xiaolai Zhou^{1,*} , Mieu Brooks¹, Peizhou Jiang¹, Shunsuke Koga¹, Aamir R Zuberi², Matthew C Baker¹, Tammee M Parsons¹, Monica Castanedes-Casey¹, Virginia Phillips¹, Ariston L Librero¹, Aishe Kurti¹, John D Fryer¹, Guojun Bu¹, Cathleen Lutz², Dennis W Dickson^{1,**} , & Rosa Rademakers^{1,3,4,***} 

Abstract

Progranulin (PGRN) and transmembrane protein 106B (TMEM106B) are important lysosomal proteins implicated in frontotemporal lobar degeneration (FTLD) and other neurodegenerative disorders. Loss-of-function mutations in progranulin (*GRN*) are a common cause of FTLD, while *TMEM106B* variants have been shown to act as disease modifiers in FTLD. Overexpression of TMEM106B leads to lysosomal dysfunction, while loss of Tmem106b ameliorates lysosomal and FTLD-related pathologies in young *Grn*^{-/-} mice, suggesting that lowering TMEM106B might be an attractive strategy for therapeutic treatment of FTLD-GRN. Here, we generate and characterize older *Tmem106b*^{-/-}*Grn*^{-/-} double knockout mice, which unexpectedly show severe motor deficits and spinal cord motor neuron and myelin loss, leading to paralysis and premature death at 11–12 months. Compared to *Grn*^{-/-}, *Tmem106b*^{-/-}*Grn*^{-/-} mice have exacerbated FTLD-related pathologies, including microgliosis, astrogliosis, ubiquitin, and phospho-Tdp43 inclusions, as well as worsening of lysosomal and autophagic deficits. Our findings confirm a functional interaction between Tmem106b and Pgrn and underscore the need to rethink whether modulating TMEM106B levels is a viable therapeutic strategy.

Keywords frontotemporal lobar degeneration; lysosomes; progranulin; Tdp-43; Tmem106b

Subject Categories Molecular Biology of Disease; Neuroscience

DOI 10.15252/embr.202050197 | Received 16 February 2020 | Revised 26 June 2020 | Accepted 14 July 2020 | Published online 5 August 2020

EMBO Reports (2020) 21: e50197

See also: **T Feng et al**, **G Werner et al** and **EL Clayton & AM Isaacs** (October 2020)

Introduction

Frontotemporal lobar degeneration (FTLD) is the second most common dementia in people under the age of 65 (Bird *et al*, 2003; Rademakers *et al*, 2012). Clinically, it is characterized by prominent changes in personality, behavior abnormalities, or language difficulties due to progressive neurodegeneration in the frontal and temporal lobes and subcortical regions of the brain (Seltman & Matthews, 2012). Pathologically, nearly half of the FTLD cases have abnormal inclusions composed of TAR DNA-binding protein of 43 kDa (TDP-43) (FTLD-TDP) (Mackenzie *et al*, 2009) and progranulin (PGRN) haploinsufficiency due to heterozygous loss-of-function mutations in the progranulin gene (*GRN*) is a major cause of FTLD-TDP (Rademakers *et al*, 2012).

Progranulin is an evolutionarily conserved secreted glycoprotein involved in multiple processes including inflammation, wound healing, and tumorigenesis (Chitramuthu *et al*, 2017). Recent studies have suggested novel functions of PGRN in lysosomes. Complete loss of PGRN leads to neuronal ceroid lipofuscinosis (NCL), a lysosomal storage disease (Smith *et al*, 2012; Almeida *et al*, 2016; Huin *et al*, 2020). Although primary trafficking pathways of PGRN are not completely clear, cell biologic studies demonstrated that PGRN can be either sorted intracellularly from ER/Golgi or taken up extracellularly and targeted to lysosomes through sortilin (Hu *et al*, 2010) and prosaposin (Zhou *et al*, 2015) pathways, where it undergoes proteolytic processing into stable granulin peptides (Holler *et al*, 2017; Lee *et al*, 2017; Zhou *et al*, 2017b). Moreover, PGRN has been implicated in regulation of multiple lysosomal enzymes, including cathepsin D (Beel *et al*, 2017; Valdez *et al*, 2017; Zhou *et al*, 2017a; Butler *et al*, 2019) and β -glucosidase (GBA) (Jian *et al*, 2016; Arrant *et al*, 2019; Zhou *et al*, 2019; Valdez *et al*, 2020). Loss of PGRN in mice consistently leads to multiple FTLD-related pathologies, including microgliosis, astrogliosis, and ubiquitin-positive inclusions (Ahmed

1 Department of Neuroscience, Mayo Clinic, Jacksonville, FL, USA

2 The Rare and Orphan Disease Center, JAX Center for Precision Genetics, Bar Harbor, ME, USA

3 Applied and Translational Neurogenomics, VIB Center for Molecular Neurology, VIB, Antwerp, Belgium

4 Department of Biomedical Sciences, University of Antwerp, Antwerp, Belgium

*Corresponding authors. Tel: +1 904 953 1085; Fax: +1 904 953 7370; E-mail: zhou.xiaolai@mayo.edu

**Corresponding authors. Tel: +1 904 953 7137; Fax: +1 904 953 7117; E-mail: dickson.dennis@mayo.edu

***Corresponding authors. Tel: +1 904 953 6279; Fax: +1 904 953 7370; E-mail: rademakers.rosa@mayo.edu

et al, 2010; Yin et al, 2010a,b; Martens et al, 2012), with reports of possible Tdp-43 pathology in some, but not all, models (Ahmed et al, 2010; Yin et al, 2010b; Wils et al, 2012).

TMEM106B is a type II transmembrane protein with an unknown function (Lang et al, 2012). Like PGRN, TMEM106B is mainly localized to lysosomes (Nicholson & Rademakers, 2016). Genetic studies have established *TMEM106B* variants as major modifiers of disease risk in FTLN with *GRN* mutations (FTLN-*GRN*) (Van Deerlin et al, 2010; Finch et al, 2011; Pottier et al, 2018). Specifically, individuals with *GRN* mutations who also carry a *TMEM106B* “protective” haplotype have ~ 50% lower odds of developing FTLN symptoms as compared to carriers of the “risk” haplotype (Finch et al, 2011; Pottier et al, 2018). Notably, the same *TMEM106B* haplotype has been shown to modify disease risk or presentation in other neurodegenerative diseases, such as Alzheimer’s disease and hippocampal sclerosis (Rutherford et al, 2012; Murray et al, 2014). In addition, *TMEM106B* haplotypes have also been associated with healthy aging (Rhinn & Abeliovich, 2017; Ren et al, 2018; Li et al, 2020).

While it remains a topic of active research to determine the specific genetic variant(s) on the *TMEM106B* haplotype responsible for the disease-modifying effect, multiple studies have suggested that the “risk” haplotype is associated with higher protein levels of TMEM106B as compared to the “protective” haplotype (Van Deerlin et al, 2010; Nicholson et al, 2013; Gallagher et al, 2017). In line with this notion, *in vitro* studies showed that increased TMEM106B protein levels lead to a multitude of lysosomal dysfunctions, such as enlarged lysosomal size, reduced lysosomal pH, and deficits in endolysosomal trafficking (Nicholson & Rademakers, 2016). Moreover, increased TMEM106B levels were reported in the brains of *Grn*^{-/-} mice (Zhou et al, 2017d), and TMEM106B was increased in FTLN-*GRN* autopsy brains (Busch et al, 2013). Overexpression of TMEM106B further exacerbated the FTLN-related pathologies, such as lipofuscin and lysosome dysfunction in brains of *Grn*^{-/-} mice (Zhou et al, 2017d). Intriguingly, loss of Tmem106b in *Grn*^{-/-} mice ameliorated both lysosomal and FTLN-related phenotypes in *Grn*^{-/-} mice (Klein et al, 2017), suggesting that lowering TMEM106B levels might serve as an attractive strategy for therapeutic targeting of FTLN-*GRN*. Other studies, however, failed to observe significant benefits from loss of Tmem106b in heterozygous *Grn*^{+/-} mice (Arrant et al, 2018) or in *C9orf72*-repeat overexpressing mice, a mouse model for another type of FTLN-TDP, where genetic studies had also identified a disease-modifying effect for *TMEM106B* haplotypes (Nicholson et al, 2018).

To further investigate the role of TMEM106B in FTLN-*GRN*, we generated *Tmem106b*^{-/-}*Grn*^{-/-} mice from two different *Tmem106b*^{-/-} mouse lines. To our surprise, instead of the expected benefits, loss of Tmem106b remarkably exacerbated FTLN-related pathologies in the brain and spinal cord of *Grn*^{-/-} mice, with increased gliosis and ubiquitin-positive inclusions, as well as lysosomal and autophagic dysfunctions, ultimately resulting in paralysis.

Results and Discussion

Loss of Tmem106b results in motor deficits in *Grn* knockout mice

Behavioral analyses in *Grn*^{-/-} mice have shown both motor (Petkau et al, 2012; Matsuwaki et al, 2015) and non-motor deficits, such as

social behavioral deficits, depression, anxiety, and changes in fear memory (Yin et al, 2010b; Filiano et al, 2013; Arrant et al, 2016; Petkau et al, 2016). In a previous study (Klein et al, 2017), using animals at only 4 months of age, loss of Tmem106b in *Grn*^{-/-} mice rescued FTLN-related behavioral abnormalities, including locomotor hyperactivity and disinhibition, without changes in general locomotor activity. The loss of Tmem106b also normalized lysosome protein levels and rescued retinal ganglion cell loss in young *Grn*^{-/-} mice. Phenotypes of older *Tmem106b*^{-/-}*Grn*^{-/-} mice, however, were not studied. To fill this gap, we generated *Tmem106b*^{-/-}*Grn*^{-/-} (double knockout, DKO) mice (Fig 1A). Notably, the *Tmem106b*^{-/-} mouse line used for this study was generated from the same ES cell clone (EPD0047_1_E02) from the Knockout Mouse Project (KOMP) Repository as the *Tmem106b*^{-/-} line from the previous study (Klein et al, 2017).

Unexpectedly, we observed that our *Tmem106b*^{-/-}*Grn*^{-/-} mice showed a waddling-like gait around 8 months of age with asynchronous walking of forelimbs and hindlimbs due to a slower movement of the hindlimbs. A hindlimb clasping test at 8 months found that the hindlimbs of *Tmem106b*^{-/-}*Grn*^{-/-} (DKO) mice were often held together and retracted to the abdomen (Fig 1B), leading to a significant increased clasping score as compared to WT mice ($P < 0.01$; Fig 1C). *Tmem106b*^{-/-} and *Grn*^{-/-} single knockout lines were not significantly different from WT in this test (Fig 1C). In fact, an accelerating rotarod test revealed *Tmem106b*^{-/-}*Grn*^{-/-} mice had a significant reduced latency to fall as early as 6 months of age ($P < 0.01$; Fig 1D), while no motor deficits were detected in *Grn*^{-/-} or *Tmem106b*^{-/-} mice at this age. Notably, after 8 months of age, the hindlimb weakness of the *Tmem106b*^{-/-}*Grn*^{-/-} mice rapidly progressed, and around 11 months, the *Tmem106b*^{-/-}*Grn*^{-/-} mice were completely paralyzed (Movie EV1) and started to die (Fig 1E). Since Klein et al (2017) only followed their mice up to 7 months in their study, this might explain why the motor deficit phenotypes were not detected in their *Tmem106b*^{-/-}*Grn*^{-/-} mice.

Importantly, in our previous study, we determined that our *Tmem106b*^{-/-} mice had an undefined N-terminal fragment, likely a fusion product of the Tmem106b N-terminus with part of the LacZ protein, resulting from the gene trap design (Nicholson et al, 2018). Using an optimized Western blot protocol, we now also show that these animals have 5–10% residual full-length Tmem106b protein expression (Fig EV1). To exclude that the motor deficits observed in our *Tmem106b*^{-/-}*Grn*^{-/-} mice were related to the N-terminal fragments, we generated a CRISPR *Tmem106b*^{-/-} mouse line with complete loss of Tmem106b (Fig EV2C–E), which we also crossed with *Grn*^{-/-} mice. The CRISPR *Tmem106b*^{-/-}*Grn*^{-/-} mice developed similar motor deficits, such as waddling-like gait, as early as 4.5 months (Movie EV2) and paralysis followed by death around 7 months (Fig EV2F), thus excluding a significant contribution from the N-terminal residual fragments in the observed pathologies and suggesting that the residual expression of a small amount of full-length Tmem106b might have been sufficient to delay disease phenotypes by several months.

Loss of Tmem106b leads to motor neuron death and myelin degeneration in *Grn* knockout mice

To investigate the cause of the limb paralysis observed in our *Tmem106b*^{-/-}*Grn*^{-/-} mice, we examined motor neurons and myelin

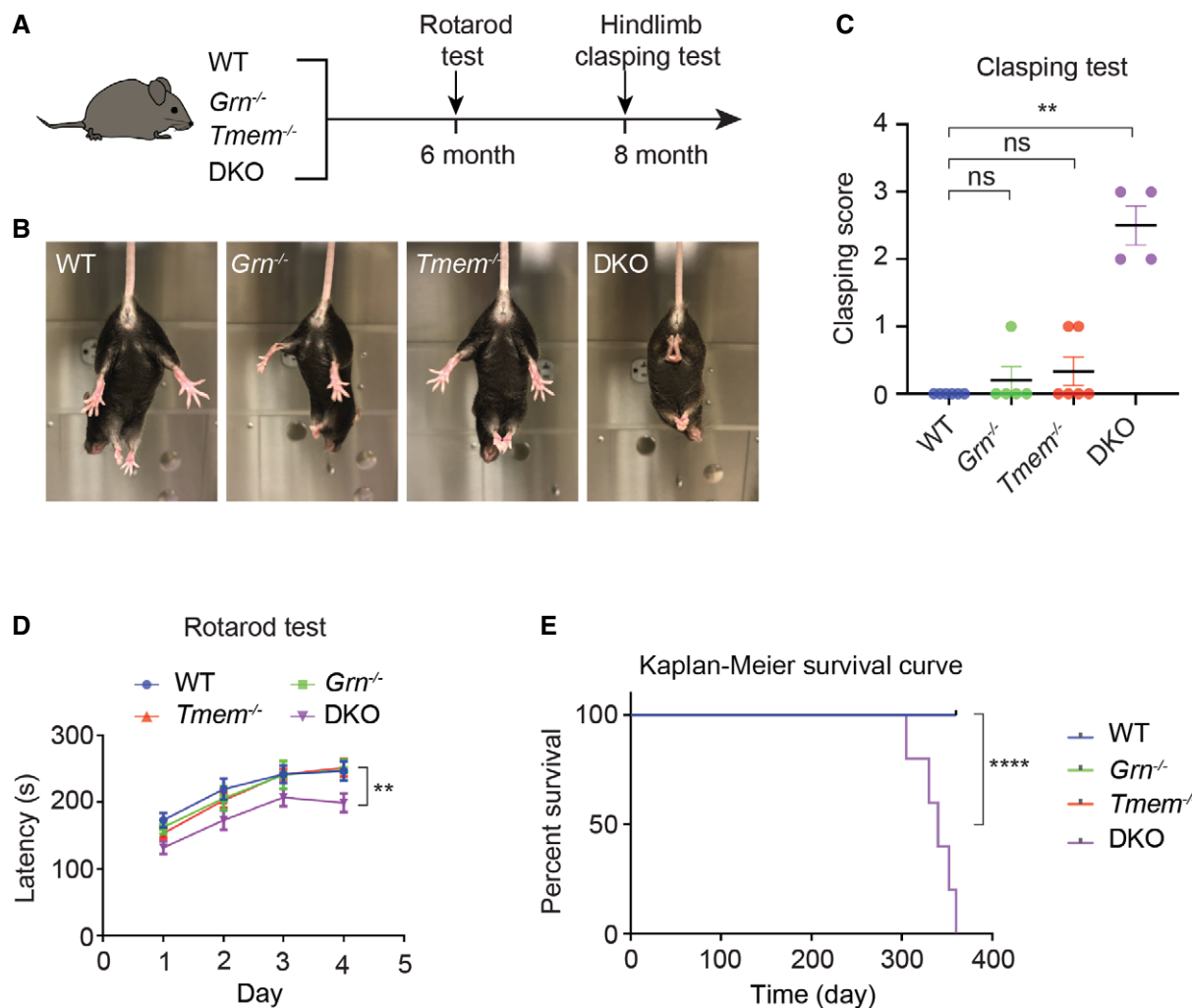


Figure 1. Motor deficits in *Grn* and *Tmem106b* double knockout mice.

A Illustration of the mouse genotypes and timeline of the behavioral tests.

B Representative photographs of the hindlimb clasping test from four different genotypes: wild-type (WT), *Grn* knockout (*Grn*^{-/-}), *Tmem106b* knockout (*Tmem*^{-/-}), and *Grn* and *Tmem106b* double knockout (DKO) mice at 8 months of age. A DKO mouse shows the stereotypic clasping response with hindlimbs retracted to the abdomen (right), while a WT (left), *Grn*^{-/-} (left middle), and *Tmem*^{-/-} animal (right middle) shows a normal response with hindlimbs splayed outwards.

C Scoring of clasping response according to hindlimb position and time. Graph represents the mean ± SEM. Data were analyzed by one-way ANOVA followed by Kruskal–Wallis test. ns, not significant, ***P* < 0.01, *n* = 6 in WT, *Grn*^{-/-} and *Tmem*^{-/-}, *n* = 4 in DKO.

D Rotarod test shows DKO mice (at 6 months of age) have significantly reduced latency to fall as compared to WT (at 6 months of age; ***P* < 0.01). Graph represents the mean ± SEM. Data were analyzed by one-way ANOVA followed by Fisher's LSD test (*n* = 6 in WT, *Grn*^{-/-}, and *Tmem*^{-/-}, *n* = 4 in DKO).

E Kaplan–Meier survival plots for four different genotypes: wild-type (WT), *Grn* knockout (*Grn*^{-/-}), *Tmem106b* knockout (*Tmem*^{-/-}), and *Grn* and *Tmem106b* double knockout (DKO) mice. DKO shows a significant reduction in survival (median survival = 340 days) to WT, *Grn*^{-/-}, and *Tmem*^{-/-} (*n* = 6 in WT, *Grn*^{-/-}, and *Tmem*^{-/-}, *n* = 5 in DKO, *P* < 0.0001, log-rank test). WT, *Grn*^{-/-}, and *Tmem*^{-/-} curves are overlapping.

in the spinal cord. In line with the rotarod test, we observed a significant loss (~ 20%, *P* < 0.05) of motor neurons in the anterior horn of the spinal cord in 11- to 12-month-old *Tmem106b*^{-/-} *Grn*^{-/-} mice, whereas age-matched *Tmem106b*^{-/-} and *Grn*^{-/-} single knockout mice did not show obvious differences in motor neuron numbers compared to WT mice (Fig 2A and B). We further examined myelin integrity in spinal cords from 11- to 12-month-old animals with luxol fast blue/periodic acid–Schiff (LFB-PAS) staining. In line with the rotarod test and motor neuron findings, *Tmem106b*^{-/-} and *Grn*^{-/-} single knockout mice did not show obvious differences in myelin

staining density and morphology compared to WT mice (Fig 2A). In contrast, we observed an overall reduction in myelin density as well as disorganized myelin fibers in the *Tmem106b*^{-/-} *Grn*^{-/-} mice (Fig 2A). Degenerated myelin debris (dense blue dots, indicated by the arrows in Fig 2A) was frequently observed in ventrolateral column. Quantification of myelin (image analysis) showed a significant loss of myelin (~ 40%; *P* < 0.01) in the ventrolateral column of the spinal cord in *Tmem106b*^{-/-} *Grn*^{-/-} mice compared to WT mice (Fig 2B). To further confirm myelin deficits, we examined the levels of two major myelin-associated proteins: 2', 3'-cyclic nucleotide

3'-phosphodiesterase (Cnp) and proteolipid protein 1 (Plp1) by Western blot. Consistent with LFB-PAS staining, a significant reduction of both Cnp (~ 25%; $P < 0.01$) and Plp1 (~ 40%; $P < 0.05$) was observed in *Tmem106b*^{-/-}*Grn*^{-/-} mice, but not in *Grn*^{-/-} or *Tmem106b*^{-/-} single knockout mice or WT mice (Fig 2D–F). Finally, we performed electronic microscopic studies and confirmed the presence of myelin degeneration in the spinal cord of the *Tmem106b*^{-/-}*Grn*^{-/-} mice (Fig 2C). We did not detect degenerated myelin in spinal cords of WT mice (Fig 2C), *Tmem106b*^{-/-} or *Grn*^{-/-} mice. Interestingly, we did not detect obvious myelin changes and neuronal loss in the brain in any of the mouse lines (Fig EV3). The resistance to myelin loss and neuronal loss in the brain could be due to the higher residual *Tmem106b* expression in brain (~ 10% vs ~ 5% spinal cord; Fig EV1) or a difference in susceptibility to *Tmem106b* loss in spinal cord as compared to brain. Importantly, neither motor neuron loss nor myelin degeneration in spinal cord is commonly seen in FTL-GRN patients. This difference between our mouse models and human disease might be due to undefined biological differences between mice and humans or from the fact that FTL-GRN patients still have 50% PGRN expression (and unknown levels of functional TMEM106B).

Loss of *Tmem106b* exacerbates FTL-GRN-related pathologies in *Grn* knockout mice

It is known that neuroinflammation plays an important role in multiple neurodegenerative diseases, including FTL-GRN (Bright *et al*, 2019). To investigate the role of neuroinflammation in the *Tmem106b*^{-/-}*Grn*^{-/-} mice, we first examined microglial and astroglial markers in anterior horn of the spinal cord. Iba-1 immunohistochemistry revealed more than a twofold increase in Iba-1-positive cells in single knockout *Grn*^{-/-} mice compared to WT mice (Fig 3A and C). In addition, microglia had morphologic differences; they more often had an amoeboid shape rather than a ramified shape (Fig 3A). These changes in *Grn*^{-/-} spinal cord were greatly enhanced in *Tmem106b*^{-/-}*Grn*^{-/-} mice, even though the loss of *Tmem106b* alone did not significantly increase Iba-1-positive cells (Fig 3A and C). Similarly, loss of *Tmem106b* in the *Grn*^{-/-} background strongly enhanced the number of Gfap-positive cells and Gfap immunoreactivity burden compared to WT mice or single knockout mice (Fig 3B and D). Notably, a similar increase in activation of microglia and astroglia was observed in posterior horn gray matter and to a lesser degree in the lateral column of the white matter (Fig 3C and D). The gliosis in both white matter and gray matter of the spinal cord in *Tmem106b*^{-/-}*Grn*^{-/-} mice mirrors neuronal loss and myelin degeneration in this area (Fig 2).

We next evaluated brain sections and also found microgliosis and astrogliosis in brains of *Grn*^{-/-} mice, especially in brainstem regions, such as the midbrain (Fig EV4A–D). In line with a previous report on *Grn*^{-/-} mice (Ahmed *et al*, 2010), there was relative sparing of the cortex and hippocampus. We also observed increased microgliosis and astrogliosis in *Grn*^{-/-} cerebellum, especially in the white matter (Fig EV4A–D). In single knockout *Tmem106b*^{-/-} mice, modest increases in microgliosis were also observed in midbrain and cerebellum, but not in cortex or hippocampus, and no significant changes in astroglia activation were observed in all four regions (Fig EV4A–D). However, similar to the findings in the spinal cord, *Tmem106b*^{-/-}*Grn*^{-/-} had significantly more microgliosis and

astrogliosis in these brain regions (Fig EV4A–D). Notably, the enhancement of the gliosis in *Grn*^{-/-} by the additional loss of *Tmem106b* followed a similar region specificity as the gliosis in *Grn*^{-/-} (midbrain > cerebellum > cortex > hippocampus) (Ahmed *et al*, 2010), suggesting that synergistic effects of loss of *Grn* and *Tmem106b* on gliosis are driven or primed by loss of *Grn*.

Of note, the increased microgliosis and astrogliosis observed in the spinal cord may have also contributed to the motor deficits in our *Tmem106b*^{-/-}*Grn*^{-/-} mice. Activated glial cells can contribute to neuronal dysfunction and survival through the release of toxic cytokines or through enhanced synaptic pruning (Kao *et al*, 2017). Similarly, microgliosis and astrogliosis observed in midbrain and cerebellum may have contributed to the hindlimb clasping phenotype (Lalonde & Strazielle, 2011). Moreover, activated glial cells could aggravate the myelin degeneration, thereby influencing motor function (Kempuraj *et al*, 2016).

Importantly, in addition to gliosis, pTDP-43 inclusion formation is another consistent pathological hallmark of FTL-GRN (Neumann *et al*, 2006). It is debated, however, whether *Grn*^{-/-} mice also develop Tdp-43 pathology (Ahmed *et al*, 2010; Yin *et al*, 2010b; Ward *et al*, 2014). Intriguingly, we were able to detect pTdp-43 inclusions in the neuropil and to a lesser extent in cytoplasm of neurons in the brainstem of *Tmem106b*^{-/-}*Grn*^{-/-} mice, but not in WT or single knockout *Tmem106b* and *Grn* mice (Fig 3E–G). Notably, pTdp-43 pathology was not observed in spinal cord, although spinal cords had more severe pathologies, including anterior horn motor neuron loss and myelin degeneration. The lack of pTdp-43 in the spinal cord is intriguing given that in FTL-GRN patients, TDP-43 pathology often co-occurs with neuronal loss and is believed to contribute to the neuronal loss, even though direct evidence supporting a causative effect of TDP-43 pathology on neuronal degeneration is still missing. The separation of Tdp-43 pathology from neurodegeneration in the spinal cord and brain of *Tmem106b*^{-/-}*Grn*^{-/-} mice suggests that at least in this model, Tdp-43 pathology might not be essential for neuronal loss.

Loss of *Tmem106b* enhances lysosomal–autophagy deficits in *Grn* knockout mice

Both *Pgrn* and *Tmem106b* are lysosomal proteins known to play important roles in maintaining proper lysosomal function (Nicholson & Rademakers, 2016; Paushter *et al*, 2018). It is also known that lysosomal and autophagic deficits can lead to myelin degeneration and are associated with motor neuron degeneration and motor deficits (Burk & Pasterkamp, 2019; Belgrad *et al*, 2020). To investigate lysosomal function and autophagy, we first examined protein levels of Lamp1 and Lc3 in spinal cord. An increase in Lamp1 protein level is often associated with lysosomal dysfunction (Zhou *et al*, 2017c; Wiwatpanit *et al*, 2018), and an elevated Lc3 II/I ratio is associated with either increased autophagy initiation or reduced autophagosome clearance by fusion with the lysosome (Klionsky *et al*, 2016). Protein analysis revealed that *Grn*^{-/-}, but not *Tmem106b*^{-/-} mice, had almost fourfold increased Lamp1 protein levels compared to WT mice (Fig 4A and B; $P < 0.01$). Importantly, *Tmem106b*^{-/-}*Grn*^{-/-} mice had even greater Lamp1 protein levels (Fig 4A and B; $P < 0.001$). Similarly, *Tmem106b*^{-/-}*Grn*^{-/-} mice also significantly increased Lc3 II/I ratios (Fig 4A and C; $P < 0.01$). The increase in Lamp1 was confirmed by immunofluorescence staining in both

microglia and neurons (Fig 4D–F). This analysis revealed that loss of *Pgrn*, and to a lesser extent loss of *Tmem106b*, was able to induce lysosomal enlargement in both microglia and neurons and that this phenotype was significantly enhanced in *Tmem106b^{-/-}Grn^{-/-}* mice (Fig 4D, G and H). The increase in lysosomal size suggests that elevated Lc3 II/I ratio observed in Western blots in *Tmem106b^{-/-}Grn^{-/-}* mice is likely due to a reduced autophagic efflux. Finally, even

though no obvious myelin loss was observed in the brain, we also detected an increase in *Lamp1* levels and *Lc3 II/I* ratio, as well as an increase in lysosomal size in *Tmem106b^{-/-}Grn^{-/-}* mice brain regions (Fig EV5A–H).

Ubiquitin-positive inclusions have been reported in some *Grn^{-/-}* mice and are consistently found in FTLN-GRN (Ahmed et al, 2010; Yin et al, 2010b). Similar to the distribution of activated microglia

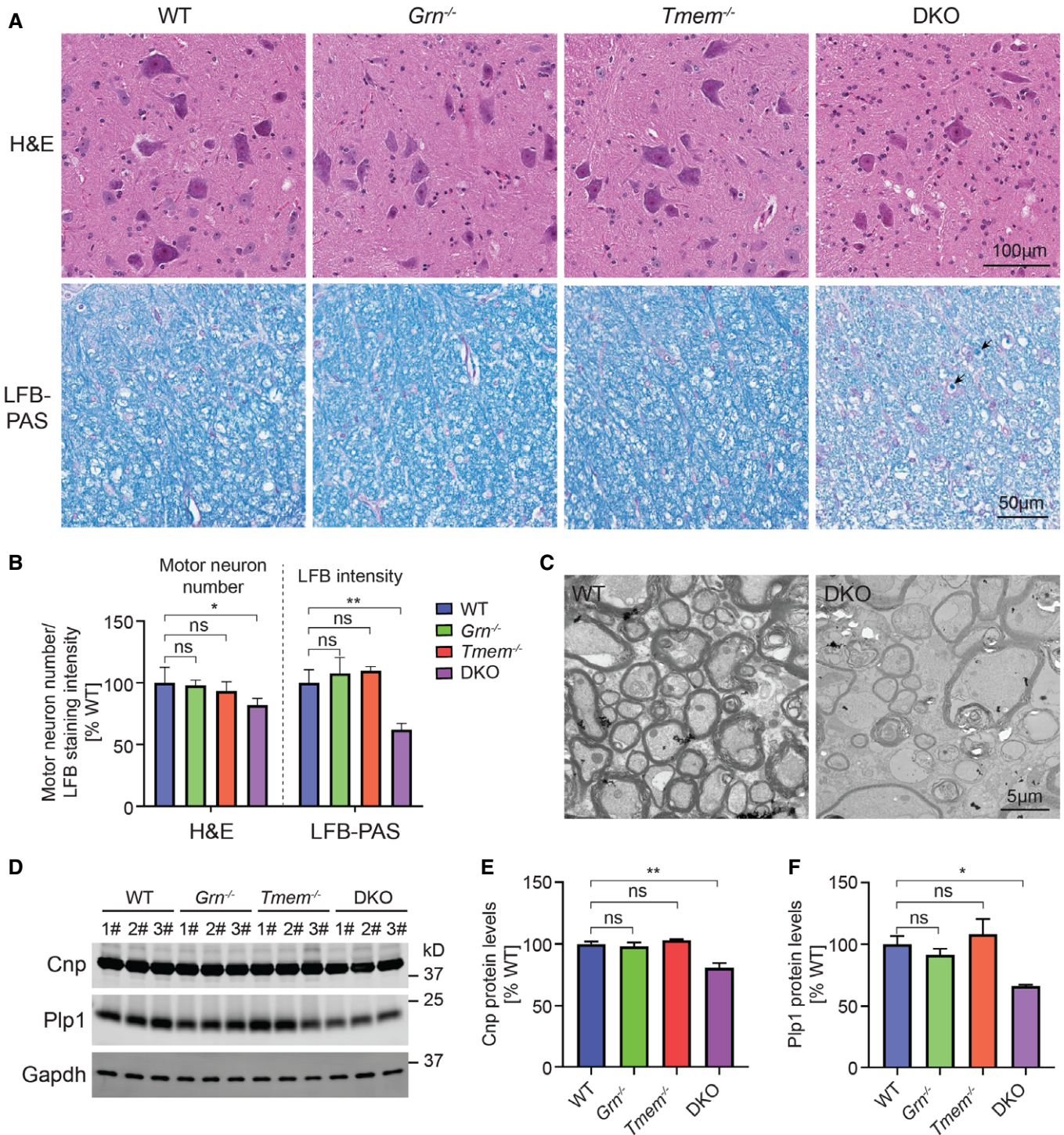


Figure 2.

Figure 2. Reduced myelination and motor neuron loss in the spinal cord of *Grn* and *Tmem106b* double knockout mice.

- A Representative images of hematoxylin and eosin (H&E) staining in anterior horn of spinal cords and Luxol fast blue and periodic acid–Schiff (LFB-PAS) staining in ventral lateral spinal fiber tract of spinal cords of 11- to 12-month-old wild-type (WT), *Grn* knockout (*Grn*^{-/-}), *Tmem106b* knockout (*Tmem*^{-/-}), and *Grn* and *Tmem106b* double knockout (DKO) mice. Arrow indicates degenerated myelin debris.
- B Quantification of the motor neuron number in anterior horn and myelin intensity (blue color) in ventral lateral spinal fiber tract of spinal cords in (A). Graph represents the mean ± SEM. Data were analyzed by one-way ANOVA followed by Tukey's multiple comparisons test (*n* = 4 per group for H&E and *n* = 3 per group for LFB-PAS). ns, not significant, **P* < 0.05, ***P* < 0.01.
- C Representative electron microscopic images of spinal cords of a WT and DKO mouse (11–12 months; *n* = 2 per group).
- D Western blots show the protein levels of myelin-related proteins: 2', 3'-cyclic nucleotide 3'-phosphodiesterase (Cnp) and proteolipid protein 1 (Plp1) and Gapdh in mice with the four indicated genotypes (11–12 months).
- E Quantification of Cnp protein levels in the four genotype groups. Graph represents the mean ± SEM. Data were analyzed by one-way ANOVA followed by Tukey's multiple comparisons test (*n* = 3 mice per group). ns, not significant, ***P* < 0.01.
- F Quantification of Plp1 protein levels in the four genotype groups. Graph represents the mean ± SEM. Data were analyzed by one-way ANOVA followed by Tukey's multiple comparisons test (*n* = 3 mice per group). ns, not significant, **P* < 0.05.

and astroglia, mild ubiquitin-positive inclusion pathology was found in the spinal cord (Fig 5A), brainstem, and cerebellum (Fig EV5I) of *Grn*^{-/-} mice. While loss of *Tmem106b* alone resulted in very subtle, if any, ubiquitin-positive inclusion pathology in spinal cord, brainstem, and cerebellum, *Tmem106b*^{-/-}*Grn*^{-/-} mice had markedly increased ubiquitin-positive inclusions in all these regions (Figs 5A and B, and EV5I). Interestingly, similar to the distribution of pTdp-43 inclusions, the vast majority of ubiquitin-positive inclusions were found in the neuropil, suggesting that pTdp-43 and ubiquitin might co-aggregate.

It is possible that both myelin loss and gliosis are due to motor neuron degeneration that can be caused by lysosomal dysfunction. In fact, both myelination deficits and microglial activation are also directly associated with lysosomal and autophagic dysfunction (Faust *et al*, 2010; Bosch & Kielian, 2015). Defective lysosomes release hydrolases, metabolites, and cathepsins into the cytoplasm, which can trigger glial activation (Bosch & Kielian, 2015). In addition, lysosomes are involved in plasma membrane trafficking of myelin proteins such as Plp1, a critical step in myelination (Trajkovic *et al*, 2006). Indeed, lysosomal dysfunction often leads to myelination problems as demonstrated by frequent occurrence of myelination deficits in lysosomal storage diseases, including Niemann–Pick disease, Gaucher disease, and metachromatic leukodystrophy (Folkerth, 1999). Both *Pgrn* and *Tmem106b* are lysosomal resident proteins and are known to play important roles in maintaining proper lysosomal function (Nicholson &

Rademakers, 2016; Paushter *et al*, 2018). Loss of *Pgrn* has been shown to cause lysosomal dysfunction and autophagic deficits (Kao *et al*, 2017; Paushter *et al*, 2018), whereas *Tmem106b* is known to regulate lysosomal size, pH, trafficking as well as autophagy (Paushter *et al*, 2018). Importantly, recent studies reported that a *de novo* mutation in *TMEM106B* (p.D252N) can lead to hypomyelinating leukodystrophy (Simons *et al*, 2017), underscoring the importance of *Tmem106b* in myelination. Here, we observed that the loss of *Pgrn* leads to abnormalities in lysosomes and deficits in autophagy as evidenced by the elevated protein levels of Lamp1, Lc3 II/I ratio, and lysosomal enlargement. These abnormalities were enhanced by further loss of *Tmem106b*, in sharp contrast with the earlier reported normalizing effect of *Tmem106b* loss in young animals (Klein *et al*, 2017). Combined with the similar effects of loss of *Tmem106b* on other *Grn*^{-/-}-related pathologies, including microgliosis, astroglia, and ubiquitin-positive inclusions, our work strongly suggests that *Tmem106b* and *Pgrn* have converging functions in maintenance of lysosomal homeostasis and that loss of *Tmem106b* exacerbates multiple phenotypes of *Grn*^{-/-}.

Concluding remarks

Our new mouse model supports a genetic interaction between *TMEM106B* and *FTLD-GRN*. In contrast to earlier reports, our results and those published independently by two other research teams in this issue of EMBO Reports (Feng *et al*, 2020; Werner *et al*, 2020)

Figure 3. Increased gliosis and pTdp-43 in *Grn* and *Tmem106b* double knockout mice.

- A Representative images of Iba-1 immunohistochemistry staining in anterior horn of spinal cords of 11- to 12-month-old wild-type (WT), *Grn* knockout (*Grn*^{-/-}), *Tmem106b* knockout (*Tmem*^{-/-}), and *Grn* and *Tmem106b* double knockout (DKO) mice.
- B Representative images of Gfap immunohistochemistry staining in anterior horn of spinal cords of 11- to 12-month-old wild-type (WT), *Grn* knockout (*Grn*^{-/-}), *Tmem106b* knockout (*Tmem*^{-/-}), and *Grn* and *Tmem106b* double knockout (DKO) mice.
- C Quantification of Iba-1-positive cells in the four genotype groups in anterior horn (AH), posterior horn (PH), and ventrolateral white matter (WM) in (A). Graph represents the mean ± SEM. Data were analyzed by one-way ANOVA followed by Tukey's multiple comparisons test (*n* = 3 per group). ns, not significant, ***P* < 0.01, *****P* < 0.0001.
- D Quantification of Gfap-positive cells in the four genotype groups in anterior horn (AH), posterior horn (PH), and ventrolateral white matter (WM) in (B). Graph represents the mean ± SEM. Data were analyzed by one-way ANOVA followed by Tukey's multiple comparisons test (*n* = 3 per group). ns, not significant, ***P* < 0.01, ****P* < 0.001, *****P* < 0.0001.
- E Representative images of pTdp-43 immunofluorescence staining in the brainstem of 11- to 12-month-old wild-type (WT), *Grn* knockout (*Grn*^{-/-}), *Tmem106b* knockout (*Tmem*^{-/-}), and *Grn* and *Tmem106b* double knockout (DKO) mice. DKO but not WT, *Grn*^{-/-}, and *Tmem*^{-/-} brains showed neuronal and neuropil pTdp-43-positive inclusions (indicated by arrow).
- F Western blots show increased pTdp-43 protein levels in RIPA insoluble fractions of the brainstem of DKO but not *Grn*^{-/-} and *Tmem*^{-/-} (at 11–12 months).
- G Quantification of pTdp-43 protein levels in the four genotype groups in (F). Graph represents the mean ± SEM. Data were analyzed by one-way ANOVA followed by Tukey's multiple comparisons test (*n* = 3 per group). ns, not significant, ****P* < 0.0001, *****P* < 0.0001.

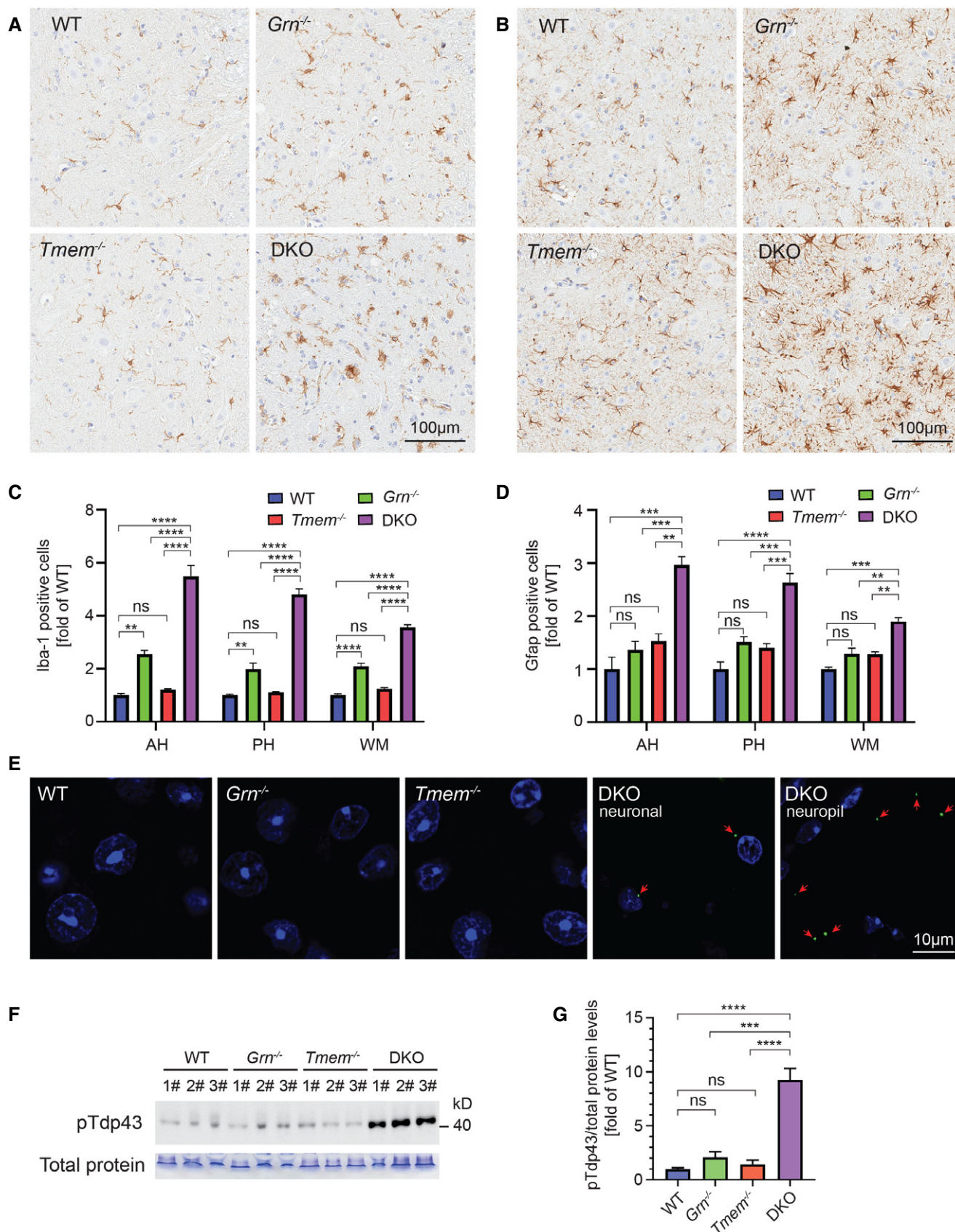


Figure 3.

suggest that loss of *Tmem106b* exacerbates lysosomal and autophagic dysfunction in *Grn*^{-/-} mice, which we found to lead to enhanced neuroinflammation, myelin, and motor neuron degeneration, ultimately leading to motor deficits and premature death. Together, our data strongly suggest that a complete loss of

TMEM106B might not be a desirable therapeutic treatment for FTLN-GRN. On the other hand, one should note that detrimental effects of complete loss of *Tmem106b* on *Grn*^{-/-} mice could happen during development. Whether a partial reduction of *Tmem106b* (for instance, by antisense oligonucleotide gene therapy) during aging

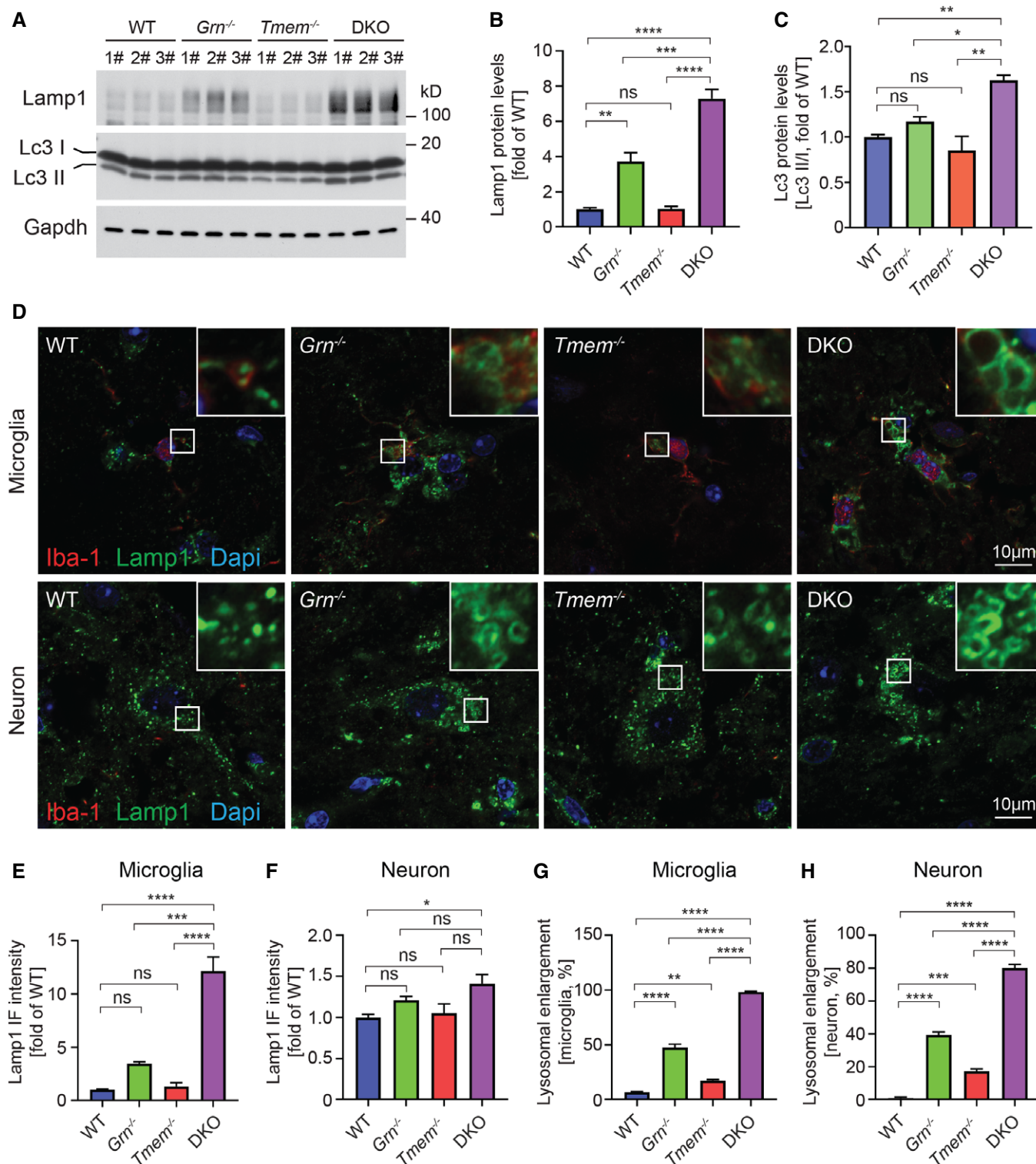
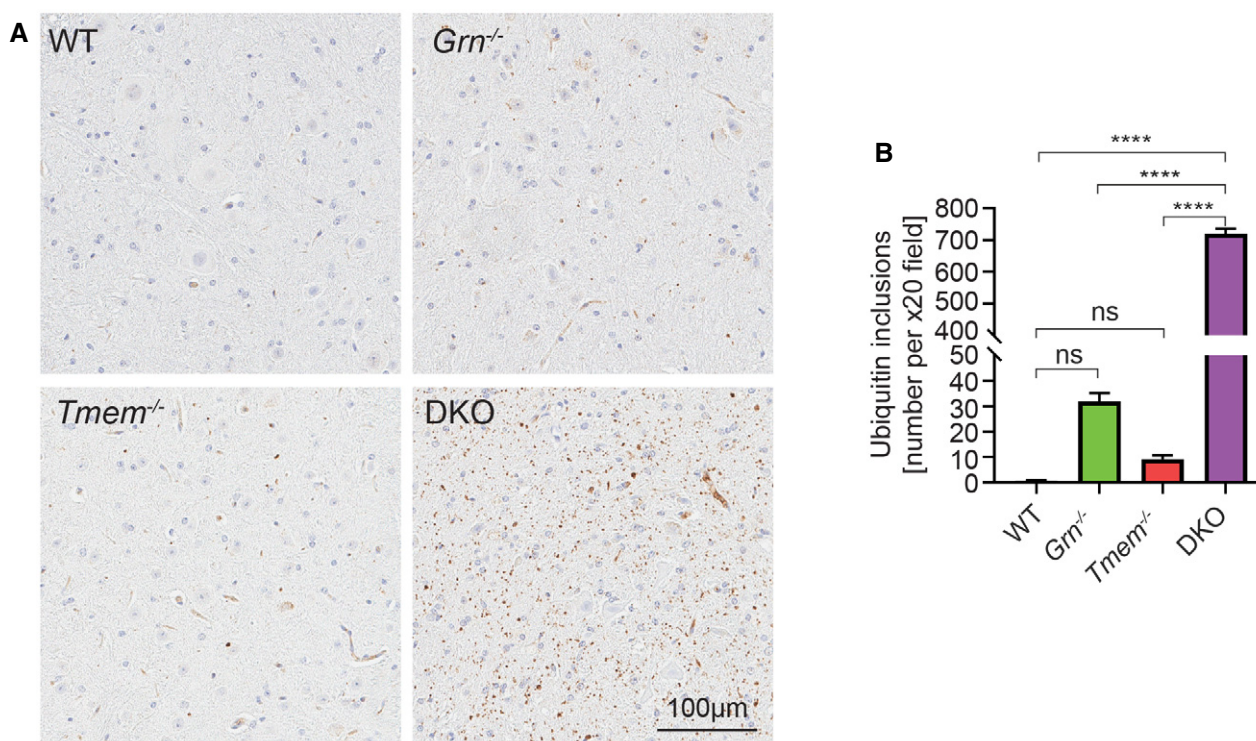


Figure 4.

Figure 4. Lysosomal deficits in the spinal cord of *Grn* and *Tmem106b* double knockout mice.

- A Western blots show the protein levels of Lamp1 and Lc3 in spinal cords of 11- to 12-month-old wild-type (WT), *Grn* knockout (*Grn*^{-/-}), *Tmem106b* knockout (*Tmem*^{-/-}), and *Grn* and *Tmem106b* double knockout (DKO) mice.
- B Quantification of Lamp1 protein levels in the four genotype groups in (A). Graph represents the mean ± SEM. Data were analyzed by one-way ANOVA followed by Tukey's multiple comparisons test (*n* = 3 mice per group). ns, not significant, ***P* < 0.01, ****P* < 0.001, *****P* < 0.0001.
- C Quantification of Lc3 I and II protein levels (Lc3 II/I ratio) in the four genotype groups in (A). Graph represents the mean ± SEM. Data were analyzed by one-way ANOVA followed by Tukey's multiple comparisons test (*n* = 3 mice per group). ns, not significant, **P* < 0.05, ***P* < 0.01.
- D Representative images of co-immunofluorescence staining of Iba-1, Lamp1, and DAPI of the spinal cords of 11- to 12-month-old wild-type (WT), *Grn* knockout (*Grn*^{-/-}), *Tmem106b* knockout (*Tmem*^{-/-}), and *Grn* and *Tmem106b* double knockout (DKO) mice.
- E Quantification of the immunofluorescence (IF) intensity of Lamp1 in microglia cells of the four genotype groups in (D). Graph represents the mean ± SEM. Data were analyzed by one-way ANOVA followed by Tukey's multiple comparisons test (*n* = 3 mice per group). ns, not significant, ****P* < 0.001, *****P* < 0.0001.
- F Quantification of the immunofluorescence (IF) intensity of Lamp1 in motor neurons of the four genotype groups in (D). Graph represents the mean ± SEM. Data were analyzed by one-way ANOVA followed by Tukey's multiple comparisons test (*n* = 3 mice per group). ns, not significant, **P* < 0.05.
- G Quantification of microglial lysosomal enlargement in the four genotype groups (D). Graph represents the mean ± SEM. Data were analyzed by one-way ANOVA followed by Tukey's multiple comparisons test (*n* = 3 mice per group). ***P* < 0.01, *****P* < 0.0001.
- H Quantification of neuronal lysosomal enlargement in the four genotype groups (D). Graph represents the mean ± SEM. Data were analyzed by one-way ANOVA followed by Tukey's multiple comparisons test (*n* = 3 mice per group). ****P* < 0.001, *****P* < 0.0001.

**Figure 5. Increased ubiquitin-positive inclusions in the spinal cord of *Grn* and *Tmem106b* double knockout mice.**

- A Representative images of ubiquitin immunochemistry staining in spinal cords of 11- to 12-month-old wild-type (WT), *Grn* knockout (*Grn*^{-/-}), *Tmem106b* knockout (*Tmem*^{-/-}), and *Grn* and *Tmem106b* double knockout (DKO) mice.
- B Quantification of ubiquitin-positive inclusions in (A). Graph represents the mean ± SEM. Data were analyzed by one-way ANOVA followed by Tukey's multiple comparisons test (*n* = 3 mice per group). ns, not significant, *****P* < 0.0001.

remains a viable therapeutic approach in FTL-GRN and related diseases will require further investigation. In addition, a deeper mechanistic understanding of TMEM106B and PGRN function within lysosomes and more human studies identifying consequences of functional variant(s) on the *TMEM106B* haplotype, including a possible loss-of-function effect of the coding variant T185 located on the risk haplotype, will be important and may aid in future therapeutic designs.

Materials and Methods

Mouse lines

C57BL/6N *Tmem106b*^{-/-} mice were originally generated at the KOMP Repository at the University of California, Davis, by knocking-in a lacZ gene trap between the first two coding exons (exons 3 and 4) of the mouse *Tmem106b* gene as described (Nicholson

et al, 2018). C57BL/6J *Grn*^{-/-} mice (Kao et al, 2011) were a generous gift from Dr. Robert Farese, Harvard Medical School. *Grn* and *Tmem106b* double knockout (DKO) mice were generated by crossing *Grn*^{-/-} and *Tmem106b*^{-/-} mice. All the mouse lines were maintained on a 12-h light/dark cycle under constant temperature (22 ± 2°C) and humidity (55 ± 5%) in the animal facility at Mayo Clinic. A *Tmem106* CRISPR knockout mouse line was generated after CRISPR/Cas9-mediated targeting experiment. To distinguish this new mouse model from the original *Tmem106b*^{-/-} mouse line mentioned above, we will refer to it as the *Tmem106b* CRISPR knockout line. This *Tmem106b* CRISPR knockout line, JR 031030 (C57BL/6J-*Tmem106b*^{em6.Lutzy/J} Jackson Laboratory, Bar Harbor, ME), contains a 108 nt deletion that includes 80 nt of distal intron 6 and 28 nt of the 5' end of exon 7. The mutation is predicted to result in a frameshift beginning at Q195 and premature termination (Fig EV2A and B). All animal experiments were approved by the Mayo Clinic Institutional Animal Care and Use Committee and the Jackson Laboratory Institutional Animal Care and Use Committee. The ages of the mice are described in each experiment. All experimental mice were chosen randomly. Male and female mice were used, and the sex of the mice in each experiment was matched between conditions and genotypes. For all animal experiments, investigators were blinded.

Assessment of mouse motor phenotypes

Rotarod test

Mice were placed on the accelerating rotarod apparatus (Ugo Basile) for 16 trials (four trials on four consecutive days) with a 30- to 60-min rest interval between trials. Each trial continued for a maximum of 10 min, during which the rod accelerated linearly from 4 to 40 rpm. The amount of time (latency) to fall from the rod (approximately six inches off-ground) was recorded for each mouse in each trial. Soft padding material was placed under the rod to cushion the fall. The examiners were blinded for the test.

Hindlimb clasping test

The hindlimb clasping test was performed as described (Guyenet et al, 2010). Briefly, mice were lifted by the tail end. The hindlimb position was observed for 10 s. The clasping scores from 0 to 3 were assigned based on the hindlimb retraction and time. A score of 0 was assigned if both hindlimbs were consistently splayed outward, away from the abdomen; a score of 1 was assigned if one hindlimb was retracted toward the abdomen for more than 5 s; a score of 2 was assigned if both hindlimbs were partially retracted toward the abdomen for more than 5 s; and a score of 3 was assigned when both hindlimbs were entirely retracted and touching the abdomen for more than 5 s. Mice were placed back into their cage afterward, and the hindlimb clasping score was recorded. The examiners were blinded to genotype for the test.

Animal harvesting and tissue preparation

Mice were euthanized by CO₂ asphyxiation. Brains and spinal cords were immediately dissected. One half of the brain was fixed in ice-cold 4% paraformaldehyde (PFA) for histologic analyses, and the other brain hemisphere was frozen in liquid nitrogen for

biochemical analyses. For spinal cords, the lumbar segments were harvested for both histological and biochemical studies.

Brain and spinal cord tissues for the histology analysis were further processed and embedded in paraffin following standard histopathologic procedures.

Brain and spinal cord tissues for Western blot analysis were homogenized in radioimmunoprecipitation assay (RIPA) buffer (Boston BioProducts) supplemented with protease inhibitors at a ratio of 1:20 (1 mg tissues and 20 µl RIPA). The supernatant was collected after centrifugation at 20,817 g for 15 min at 4°C. Protein concentration was measured using the BCA assay (Thermo Fisher Scientific).

Mice for electron microscopy (EM) studies were transcardially perfused with EM fixation buffer containing 2% glutaraldehyde and 2% PFA in 0.1 M PBS. Lumbar segments of the spinal cords were then dissected and fixed in EM fixation buffer for 24 h at 4°C.

Histology studies

Hematoxylin and eosin (H&E) staining

Mouse tissues were fixed with 4% formaldehyde. After dehydration with 70% ethanol, tissues were embedded in paraffin and cut at 5 µm thickness and mounted on glass slides. Following deparaffinization with xylene and ethanol (100, 95, 80%) and rehydration with tap water, the slides were then stained in hematoxylin for 3 min, destained with acid ethanol and rinsed with tap water, and then stained with eosin for 30 s. Slides were then dehydrated with ethanol and xylene and mounted. Slides were scanned with the Aperio ScanScope AT2 Slide Scanner (Aperio, Vista, CA). For quantification of spinal cord anterior horn motor neurons and neurons in the motor cortex, four entire anterior horn regions and four random images from each sample were captured at the 20× magnification, respectively. The anterior horn motor neurons and cortical neurons were manually counted using ImageJ software (NIH).

Immunohistochemistry and immunofluorescence staining

For immunohistochemistry staining of Iba-1, Gfap, and ubiquitin, paraffin-embedded mouse brain and spinal cord were sectioned at 5 µm thickness and mounted on glass slides. The tissue sections were deparaffinized in xylene and rehydrated in a graded series of alcohols. Antigen retrieval was performed by steaming in deionized water for 30 min, and endogenous peroxidase activity was blocked by incubation in 0.03% hydrogen peroxide. Tissue sections were then immunostained with anti-Iba1 (019-19741, Wako, 1:3,000), anti-Gfap (Pu020-UP, BioGenex, 1:2,500), and anti-ubiquitin (MAB1510, Millipore, 1:55,000) antibodies using the Thermo Scientific Autostainer 480S (Fremont, CA) and the DAKO EnVision + HRP system. The stained slides were then dehydrated, coverslipped, and scanned with the Aperio ScanScope AT2 Slide Scanner (Aperio, Vista, CA). For quantification, four random images from each sample were captured at the 20× magnification. Iba-1- and Gfap-positive cells and ubiquitin-positive inclusions were manually counted using ImageJ software (NIH).

Immunofluorescence staining was performed as previously described (Zhou et al, 2015). Briefly, antigen retrieval was performed by microwaving in citrate buffer (pH 6.0) for 18 min after deparaffinization. To block the autofluorescence, tissue slides were incubated with 0.1% Sudan Black B (Spectrum Chemical) in 70%

ethanol for 20 min at room temperature before immunostaining. Slides were then blocked and incubated with mouse anti-phospho-TDP43 (phospho-409/410, TIP-PTD-M01, Cosmo Bio, 1:500), rabbit anti-Iba1 (019-19741, Wako, 1:500), and rat anti-Lamp1 (ab25245, BD Biosciences, 1:250) overnight followed by incubation with donkey anti-mouse Alexa 488 secondary antibody. Hoechst 33258 was used to stain nuclei. Images were acquired on a Zeiss LSM700 laser scanning confocal microscope under a 63× oil-objective lens with 2.0 zoom-in using an AirScan detector. The immunofluorescence intensity of LAMP1 and assessment of lysosomes enlargement were quantified as in previous studies (Zhou *et al*, 2017c,d). Briefly, for the quantification of immunofluorescence intensity of LAMP1, in each animal at least 12 randomly captured cells (microglia/neuron) were quantified using ImageJ (NIH). For the quantification of enlarged lysosomes, the lysosomes were visualized by anti-LAMP1 staining. For each animal, at least 50 (for neuron) or 100 (for microglia) randomly captured cells were examined using ImageJ (NIH). The number of total cells, as well as cells with enlarged lysosomes (diameter > 1.0 μm), was counted. The average values from each animal were used for the statistical analysis.

Luxol fast blue-periodic acid-Schiff staining

Paraffin-embedded mouse brain and spinal cord sections were deparaffinized and hydrated as described above. Slides were incubated in LFB solution (10% Luxol fast blue dissolved in 95% ethanol and 5% acetic acid) for 2 h at room temperature. The slides were further incubated in 0.5% periodic acid solution for 5 min and Schiff's solution for 15 min. Stained slides were then washed with 95% ethanol and distilled water. Washed slides were incubated in a saturated lithium carbonate solution for about 3 min and then washed once in distilled water. Stained brain slides were dehydrated in ethanol and xylene and mounted with permanent mounting media. Images were captured using an Aperio ScanScope AT2 Slide Scanner (Aperio, Vista, CA). For quantification, the corticospinal tract was annotated using ImageScope-11.2 and analyzed in Spectrum-11.2 (Aperio Technologies) using a custom-designed color deconvolution algorithm to detect only LFB-stained pixels (positive pixels). The LFB-positive ratio was calculated as a percentage ratio of the area of positive pixels to the total area of the annotated region.

Electron microscopy

The lumbar segment of the spinal cords was dissected from the fixed spinal cord and placed in 2.5% glutaraldehyde in 0.1 M cacodylate buffer, pH 7.4 overnight. After PBS washing, tissue was post-fixed in 1% OsO₄, *en bloc*, washed three times in pure water, stained with 1% uranyl acetate and 50% ethanol, dehydrated in 70, 80, 95, and 100% ethanol and propylene oxide, and infiltrated and embedded in Epon 812 (Polysciences). Ultrathin sections were cut from the Epon 812-embedded samples by Leica Ultramicrotome, counterstained with uranyl acetate and lead citrate, and imaged with a Philips 208S electron microscope at 1,000 magnification.

Western blotting

Fifty microgram of total proteins from brain or spinal cord was mixed with 2× Novex Tris-Glycine SDS sample buffer (Cat# LC2676, Life Technologies) supplemented with 5%

β-mercaptoethanol and denatured at 95°C for 2 min. The samples were then separated in 10–12% SDS-polyacrylamide gels (Life Technologies) and transferred to Immobilon membranes (Millipore, Billerica, MA). After blocking with Odyssey blocking solution (LI-COR Biosciences) or 5% non-fat milk, the membranes were incubated with primary antibody at 4°C overnight. The next day, blots were incubated with either an HRP-conjugated secondary antibody (Promega, Madison, WI) and detected by enhanced chemiluminescence using Western Lightening Plus-ECL reagents (Perkin Elmer, Waltham, MA) or an IRDye 680/800-conjugated secondary antibody (Invitrogen) or 800 (LI-COR Biosciences) and detected by an Odyssey Infrared Imaging System (LI-COR Biosciences). Primary antibodies included the following: rabbit anti-Tmem106b [a gift from Dr. Fenghua Hu (Brady *et al*, 2014), 1:1,000], mouse anti-Cnp (MAB326, Millipore, 1:2,000), rabbit anti-Plp1 (ab28486, Abcam, 1:5,000), rat anti-Lamp1 (ab25245, BD Biosciences, 1:500), mouse anti-Gapdh (H86504M; Meridian Life Science), mouse anti-phospho-TDP43 (phospho-(409/410), TIP-PTD-M01, Cosmo Bio, 1:2,000), and rabbit anti-Lc3 (NB600-1384, Novus, 1:5,000). Bands on the Western blots were quantified using ImageJ (NIH).

Statistical analysis

In all experiments, data were expressed as mean ± SEM. One-way analysis of variance (ANOVA) followed by either a Tukey's multiple comparisons test or a Kruskal–Wallis test or a Fisher's LSD test was used to test for statistical significance between groups. Survival curves for the mice were created using the product-limit method of Kaplan and Meier, and the log-rank (Mantel–Cox) test was used to statistically test survival differences among different genotypes. All statistical analyses were performed using the GraphPad Prism 5 software (GraphPad Software, San Diego, CA). *P*-values < 0.05 were considered statistically significant.

Expanded View for this article is available online.

Acknowledgements

RR received funding from the National Institutes of Health (NIH) (grant R35 NS097261) and the Bluefield Project to Cure FTLD. The generation of the CRISPR/Cas9 *Tmem106b* knockout mouse model at The Jackson Laboratory was supported by The Center for Precision Genetics, NIH U54 OD020351, and partially supported by the Jackson Laboratory's Genetic Engineering Technologies Scientific Service. XZ is supported by a research fellowship from The Bluefield Project to Cure FTD and a Developmental Grant from the Mayo Clinic ADRC (NIH P30 AG062677).

Author contributions

XZ designed and performed experiments and analyzed data. MB, PJ, SK, ARZ, MCB, TMP, MC-C, VP, ALL, and AK performed experiments and analyzed data. CL, JDF, GB, DWD, and RR designed experiments and analyzed data. XZ, DWD, and RR wrote the manuscript and supervised the work; all other authors edited the manuscript.

Conflict of interest

The authors declare that they have no conflict of interest.

References

- Ahmed Z, Sheng H, Xu YF, Lin WL, Innes AE, Gass J, Yu X, Wuertzer CA, Hou H, Chiba S et al (2010) Accelerated lipofuscinosis and ubiquitination in granulin knockout mice suggest a role for progranulin in successful aging. *Am J Pathol* 177: 311–324
- Almeida MR, Macario MC, Ramos L, Baldeiras I, Ribeiro MH, Santana I (2016) Portuguese family with the co-occurrence of frontotemporal lobar degeneration and neuronal ceroid lipofuscinosis phenotypes due to progranulin gene mutation. *Neurobiol Aging* 41: 200.e201–200.e205
- Arrant AE, Filiano AJ, Warmus BA, Hall AM, Roberson ED (2016) Progranulin haploinsufficiency causes biphasic social dominance abnormalities in the tube test. *Genes Brain Behav* 15: 588–603
- Arrant AE, Nicholson AM, Zhou X, Rademakers R, Roberson ED (2018) Partial Tmem106b reduction does not correct abnormalities due to progranulin haploinsufficiency. *Mol Neurodegener* 13: 32
- Arrant AE, Roth JR, Boyle NR, Kashyap SN, Hoffmann MQ, Murchison CF, Ramos EM, Nana AL, Spina S, Grinberg LT et al (2019) Impaired beta-glucocerebrosidase activity and processing in frontotemporal dementia due to progranulin mutations. *Acta Neuropathol Commun* 7: 218
- Beel S, Moisse M, Damme M, De Muynck L, Robberecht W, Van Den Bosch L, Saftig P, Van Damme P (2017) Progranulin functions as a cathepsin D chaperone to stimulate axonal outgrowth *in vivo*. *Hum Mol Genet* 26: 2850–2863
- Belgrad J, De Pace R, Fields RD (2020) Autophagy in myelinating glia. *J Neurosci* 40: 256–266
- Bird T, Knopman D, VanSwieten J, Rosso S, Feldman H, Tanabe H, Graff-Raford N, Geschwind D, Verpillat P, Hutton M (2003) Epidemiology and genetics of frontotemporal dementia/Pick's disease. *Ann Neurol* 54(Suppl 5): S29–S31
- Bosch ME, Kielian T (2015) Neuroinflammatory paradigms in lysosomal storage diseases. *Front Neurosci* 9: 417
- Brady OA, Zhou X, Hu F (2014) Regulated intramembrane proteolysis of the frontotemporal lobar degeneration risk factor, TMEM106B, by signal peptide peptidase-like 2a (SPPL2a). *J Biol Chem* 289: 19670–19680
- Bright F, Werry EL, Dobson-Stone C, Piguet O, Ittner LM, Halliday GM, Hodges JR, Kiernan MC, Loy CT, Kassiou M et al (2019) Neuroinflammation in frontotemporal dementia. *Nat Rev Neurol* 15: 540–555
- Burk K, Pasterkamp RJ (2019) Disrupted neuronal trafficking in amyotrophic lateral sclerosis. *Acta Neuropathol* 137: 859–877
- Busch JI, Martinez-Lage M, Ashbridge E, Grossman M, Van Deerlin VM, Hu F, Lee VM, Trojanowski JQ, Chen-Plotkin AS (2013) Expression of TMEM106B, the frontotemporal lobar degeneration-associated protein, in normal and diseased human brain. *Acta Neuropathol Commun* 1: 36
- Butler VJ, Cortopassi WA, Gururaj S, Wang AL, Pierce OM, Jacobson MP, Kao AW (2019) Multi-granulin domain peptides bind to pro-cathepsin D and stimulate its enzymatic activity more effectively than progranulin *in vitro*. *Biochemistry* 58: 2670–2674
- Chitramuthu BP, Bennett HPJ, Bateman A (2017) Progranulin: a new avenue towards the understanding and treatment of neurodegenerative disease. *Brain* 140: 3081–3104
- Faust PL, Kaye EM, Powers JM (2010) Myelin lesions associated with lysosomal and peroxisomal disorders. *Expert Rev Neurother* 10: 1449–1466
- Feng T, Mai S, Roscoe JM, Sheng RR, Ullah M, Zhang J, Katz II, Yu H, Xiong W, Hu F (2020) Loss of TMEM106B and PGRN leads to severe lysosomal abnormalities and neurodegeneration in mice. *EMBO Rep* 21: e50219
- Filiano AJ, Martens LH, Young AH, Warmus BA, Zhou P, Diaz-Ramirez G, Jiao J, Zhang Z, Huang EJ, Gao FB et al (2013) Dissociation of frontotemporal dementia-related deficits and neuroinflammation in progranulin haploinsufficient mice. *J Neurosci* 33: 5352–5361
- Finch N, Carrasquillo MM, Baker M, Rutherford NJ, Coppola G, DeJesus-Hernandez M, Crook R, Hunter T, Ghidoni R, Benussi L et al (2011) TMEM106B regulates progranulin levels and the penetrance of FTLD in GRN mutation carriers. *Neurology* 76: 467–474
- Folkerth RD (1999) Abnormalities of developing white matter in lysosomal storage diseases. *J Neuropathol Exp Neurol* 58: 887–902
- Gallagher MD, Posavi M, Huang P, Unger TL, Berlyand Y, Gruenewald AL, Chesi A, Manduchi E, Wells AD, Grant SFA et al (2017) A dementia-associated risk variant near TMEM106B alters chromatin architecture and gene expression. *Am J Hum Genet* 101: 643–663
- Guyenet SJ, Furrer SA, Damian VM, Baughan TD, La Spada AR, Garden GA (2010) A simple composite phenotype scoring system for evaluating mouse models of cerebellar ataxia. *J Vis Exp* 39: 1787
- Holler CJ, Taylor G, Deng Q, Kukar T (2017) Intracellular proteolysis of progranulin generates stable, lysosomal granulins that are haploinsufficient in patients with frontotemporal dementia caused by GRN mutations. *eNeuro* 4: ENEURO.0100-17
- Hu F, Padukkavidana T, Vaegter CB, Brady OA, Zheng Y, Mackenzie IR, Feldman HH, Nykjaer A, Strittmatter SM (2010) Sortilin-mediated endocytosis determines levels of the frontotemporal dementia protein, progranulin. *Neuron* 68: 654–667
- Huin V, Barbier M, Bottani A, Lobrinus JA, Clot F, Lamari F, Chat L, Rucheton B, Fluchere F, Auvin S et al (2020) Homozygous GRN mutations: new phenotypes and new insights into pathological and molecular mechanisms. *Brain* 143: 303–319
- Jian J, Zhao S, Tian QY, Liu H, Zhao Y, Chen WC, Grunig G, Torres PA, Wang BC, Zeng B et al (2016) Association between progranulin and gaucher disease. *EBioMedicine* 11: 127–137
- Kao AW, Eisenhut RJ, Martens LH, Nakamura A, Huang A, Bagley JA, Zhou P, de Luis A, Neukomm LJ, Cabello J et al (2011) A neurodegenerative disease mutation that accelerates the clearance of apoptotic cells. *Proc Natl Acad Sci USA* 108: 4441–4446
- Kao AW, McKay A, Singh PP, Brunet A, Huang EJ (2017) Progranulin, lysosomal regulation and neurodegenerative disease. *Nat Rev Neurosci* 18: 325–333
- Kempuraj D, Thangavel R, Natteru PA, Selvakumar GP, Saeed D, Zahoor H, Zaheer S, Iyer SS, Zaheer A (2016) Neuroinflammation induces neurodegeneration. *J Neurol Neurosurg Spine* 1: 1003
- Klein ZA, Takahashi H, Ma M, Stagi M, Zhou M, Lam TT, Strittmatter SM (2017) Loss of TMEM106B ameliorates lysosomal and frontotemporal dementia-related phenotypes in progranulin-deficient mice. *Neuron* 95: 281–296.e286
- Klionsky DJ, Abdelmohsen K, Abe A, Abedin MJ, Abeliovich H, Acevedo Arozena A, Adachi H, Adams CM, Adams PD, Adeli K et al (2016) Guidelines for the use and interpretation of assays for monitoring autophagy. *Autophagy* 12: 1–222
- Lalonde R, Strazielle C (2011) Brain regions and genes affecting limb-clasping responses. *Brain Res Rev* 67: 252–259
- Lang CM, Fellerer K, Schwenk BM, Kuhn PH, Kremmer E, Edbauer D, Capell A, Haass C (2012) Membrane orientation and subcellular localization of transmembrane protein 106B (TMEM106B), a major risk factor for frontotemporal lobar degeneration. *J Biol Chem* 287: 19355–19365

- Lee CW, Stankowski JN, Chew J, Cook CN, Lam YW, Almeida S, Carlomagno Y, Lau KF, Prudencio M, Gao FB et al (2017) The lysosomal protein cathepsin L is a progranulin protease. *Mol Neurodegener* 12: 55
- Li Z, Farias FHG, Dube U, Del-Aguila JL, Mihindukulasuriya KA, Fernandez MV, Ibanez L, Budde JP, Wang F, Lake AM et al (2020) The TMEM106B FTLD-protective variant, rs1990621, is also associated with increased neuronal proportion. *Acta Neuropathol* 139: 45–61
- Mackenzie IR, Neumann M, Bigio EH, Cairns NJ, Alafuzoff I, Kril J, Kovacs GG, Ghetti B, Halliday G, Holm IE et al (2009) Nomenclature for neuropathologic subtypes of frontotemporal lobar degeneration: consensus recommendations. *Acta Neuropathol* 117: 15–18
- Martens LH, Zhang J, Barmada SJ, Zhou P, Kamiya S, Sun B, Min SW, Gan L, Finkbeiner S, Huang EJ et al (2012) Progranulin deficiency promotes neuroinflammation and neuron loss following toxin-induced injury. *J Clin Invest* 122: 3955–3959
- Matsuwaki T, Kobayashi A, Mase K, Nakamura K, Nakano S, Miyoshi T, Yamanouchi K, Nishihara M (2015) Possible involvement of the cerebellum in motor-function impairment in progranulin-deficient mice. *NeuroReport* 26: 877–881
- Murray ME, Cannon A, Graff-Radford NR, Liesinger AM, Rutherford NJ, Ross OA, Duara R, Carrasquillo MM, Rademakers R, Dickson DW (2014) Differential clinicopathologic and genetic features of late-onset amnesic dementias. *Acta Neuropathol* 128: 411–421
- Neumann M, Sampathu DM, Kwong LK, Truax AC, Micsenyi MC, Chou TT, Bruce J, Schuck T, Grossman M, Clark CM et al (2006) Ubiquitinated TDP-43 in frontotemporal lobar degeneration and amyotrophic lateral sclerosis. *Science* 314: 130–133
- Nicholson AM, Finch NA, Wojtas A, Baker MC, Perkerson RB 3rd, Castanedes-Casey M, Rousseau L, Benussi L, Binetti G, Ghidoni R et al (2013) TMEM106B p. T185S regulates TMEM106B protein levels: implications for frontotemporal dementia. *J Neurochem* 126: 781–791
- Nicholson AM, Rademakers R (2016) What we know about TMEM106B in neurodegeneration. *Acta Neuropathol* 132: 639–651
- Nicholson AM, Zhou X, Perkerson RB, Parsons TM, Chew J, Brooks M, DeJesus-Hernandez M, Finch NA, Matchett BJ, Kurti A et al (2018) Loss of Tmem106b is unable to ameliorate frontotemporal dementia-like phenotypes in an AAV mouse model of C9ORF72-repeat induced toxicity. *Acta Neuropathol Commun* 6: 42
- Paushter DH, Du H, Feng T, Hu F (2018) The lysosomal function of progranulin, a guardian against neurodegeneration. *Acta Neuropathol* 136: 1–17
- Petkau TL, Neal SJ, Milnerwood A, Mew A, Hill AM, Orban P, Gregg J, Lu G, Feldman HH, Mackenzie IR et al (2012) Synaptic dysfunction in progranulin-deficient mice. *Neurobiol Dis* 45: 711–722
- Petkau TL, Hill A, Leavitt BR (2016) Core neuropathological abnormalities in progranulin-deficient mice are penetrant on multiple genetic backgrounds. *Neuroscience* 315: 175–195
- Pottier C, Zhou X, Perkerson RB 3rd, Baker M, Jenkins GD, Serie DJ, Ghidoni R, Benussi L, Binetti G, Lopez de Munain A et al (2018) Potential genetic modifiers of disease risk and age at onset in patients with frontotemporal lobar degeneration and GRN mutations: a genome-wide association study. *Lancet Neurol* 17: 548–558
- Rademakers R, Neumann M, Mackenzie IR (2012) Advances in understanding the molecular basis of frontotemporal dementia. *Nat Rev Neurol* 8: 423–434
- Ren Y, van Blitterswijk M, Allen M, Carrasquillo MM, Reddy JS, Wang X, Beach TG, Dickson DW, Ertekin-Taner N, Asmann YW et al (2018) TMEM106B haplotypes have distinct gene expression patterns in aged brain. *Mol Neurodegener* 13: 35
- Rhinn H, Abeliovich A (2017) Differential aging analysis in human cerebral cortex identifies variants in TMEM106B and GRN that regulate aging phenotypes. *Cell Syst* 4: 404–415.e405
- Rutherford NJ, Carrasquillo MM, Li M, Bisceglia G, Menke J, Josephs KA, Parisi JE, Petersen RC, Graff-Radford NR, Younkin SG et al (2012) TMEM106B risk variant is implicated in the pathologic presentation of Alzheimer disease. *Neurology* 79: 717–718
- Seltman RE, Matthews BR (2012) Frontotemporal lobar degeneration: epidemiology, pathology, diagnosis and management. *CNS Drugs* 26: 841–870
- Simons C, Dymont D, Bent SJ, Crawford J, D'Hooghe M, Kohlschutter A, Venkateswaran S, Helman G, Poll-The BT, Makowski CC et al (2017) A recurrent *de novo* mutation in TMEM106B causes hypomyelinating leukodystrophy. *Brain* 140: 3105–3111
- Smith KR, Damiano J, Franceschetti S, Carpenter S, Canafoglia L, Morbin M, Rossi G, Pareyson D, Mole SE, Staropoli JF et al (2012) Strikingly different clinicopathological phenotypes determined by progranulin-mutation dosage. *Am J Hum Genet* 90: 1102–1107
- Trajkovic K, Dhaunchak AS, Goncalves JT, Wenzel D, Schneider A, Bunt G, Nave KA, Simons M (2006) Neuron to glia signaling triggers myelin membrane exocytosis from endosomal storage sites. *J Cell Biol* 172: 937–948
- Valdez C, Wong YC, Schwake M, Bu G, Wszolek ZK, Krainc D (2017) Progranulin-mediated deficiency of cathepsin D results in FTD and NCL-like phenotypes in neurons derived from FTD patients. *Hum Mol Genet* 26: 4861–4872
- Valdez C, Ysselstein D, Young TJ, Zheng J, Krainc D (2020) Progranulin mutations result in impaired processing of prosaposin and reduced glucocerebrosidase activity. *Hum Mol Genet* 29: 716–726
- Van Deerlin VM, Sleiman PM, Martinez-Lage M, Chen-Plotkin A, Wang LS, Graff-Radford NR, Dickson DW, Rademakers R, Boeve BF, Grossman M et al (2010) Common variants at 7p21 are associated with frontotemporal lobar degeneration with TDP-43 inclusions. *Nat Genet* 42: 234–239
- Ward ME, Taubes A, Chen R, Miller BL, Sephton CF, Gelfand JM, Minami S, Boscardin J, Martens LH, Seeley WW et al (2014) Early retinal neurodegeneration and impaired Ran-mediated nuclear import of TDP-43 in progranulin-deficient FTLD. *J Exp Med* 211: 1937–1945
- Werner G, Damme M, Schludi M, Gnörich J, Wind K, Fellerer K, Wefers B, Wurst W, Edbauer D, Brendel M et al (2020) Loss of TMEM106B potentiates lysosomal and FTD-like pathology in progranulin deficient mice. *EMBO Rep* 21: e50241
- Wils H, Kleinberger G, Pereson S, Janssens J, Capell A, Van Dam D, Cuijt I, Joris G, De Deyn PP, Haass C et al (2012) Cellular ageing, increased mortality and FTLD-TDP-associated neuropathology in progranulin knockout mice. *J Pathol* 228: 67–76
- Wiwatpanit T, Remis NN, Ahmad A, Zhou Y, Clancy JC, Cheatham MA, Garcia-Anoveros J (2018) Codeficiency of lysosomal mucopolipins 3 and 1 in cochlear hair cells diminishes outer hair cell longevity and accelerates age-related hearing loss. *J Neurosci* 38: 3177–3189
- Yin F, Banerjee R, Thomas B, Zhou P, Qian L, Jia T, Ma X, Ma Y, Iadecola C, Beal MF et al (2010a) Exaggerated inflammation, impaired host defense, and neuropathology in progranulin-deficient mice. *J Exp Med* 207: 117–128
- Yin F, Dumont M, Banerjee R, Ma Y, Li H, Lin MT, Beal MF, Nathan C, Thomas B, Ding A (2010b) Behavioral deficits and progressive neuropathology in

- progranulin-deficient mice: a mouse model of frontotemporal dementia. *FASEB J* 24: 4639–4647
- Zhou X, Sun L, Bastos de Oliveira F, Qi X, Brown WJ, Smolka MB, Sun Y, Hu F (2015) Prosaposin facilitates sortilin-independent lysosomal trafficking of progranulin. *J Cell Biol* 210: 991–1002
- Zhou X, Paushter DH, Feng T, Pardon CM, Mendoza CS, Hu F (2017a) Regulation of cathepsin D activity by the FTL protein progranulin. *Acta Neuropathol* 134: 151–153
- Zhou X, Paushter DH, Feng T, Sun L, Reinheckel T, Hu F (2017b) Lysosomal processing of progranulin. *Mol Neurodegener* 12: 62
- Zhou X, Sun L, Bracko O, Choi JW, Jia Y, Nana AL, Brady OA, Hernandez JCC, Nishimura N, Seeley WW et al (2017c) Impaired prosaposin lysosomal trafficking in frontotemporal lobar degeneration due to progranulin mutations. *Nat Commun* 8: 15277
- Zhou X, Sun L, Brady OA, Murphy KA, Hu F (2017d) Elevated TMEM106B levels exaggerate lipofuscin accumulation and lysosomal dysfunction in aged mice with progranulin deficiency. *Acta Neuropathol Commun* 5: 9
- Zhou X, Paushter DH, Pagan MD, Kim D, Nunez Santos M, Lieberman RL, Overkleeft HS, Sun Y, Smolka MB, Hu F (2019) Progranulin deficiency leads to reduced glucocerebrosidase activity. *PLoS ONE* 14: e0212382